Journal of Thermal Analysis and Calorimetry (2023) 148:9963–9977
https://doi.org/10.1007/s10973-023-12378-9

Accelerated carbonation of oil-well cement blended with pozzolans and latent hydraulic materials

Eva Kuzielová[1,2] · Michal Slaný[1,3] · Matúš Žemlička[1] · Jiří Másilko[4]

Received: 9 December 2022 / Accepted: 11 July 2023 / Published online: 12 August 2023

Abstract

Accelerated carbonation of cement mixtures consisting of class G cement, silica fume, metakaolin, or blast furnace slag was studied by thermogravimetric, X-ray diffraction and Fourier transform infrared analyses for 1 year. Surface parts were fully carbonated during the first 7 days. Polymerization of amorphous hydrates due to their decalcification was observed together with the rising amount of calcium carbonates and reformation of gypsum from ettringite and monosulfate. Decalcification of clinker phases took place fast after the depletion of portlandite. Although portlandite was still present in unblended pastes, because of slower carbonation rate in the surface parts and higher C/S ratio of amorphous hydrates, the carbonation front moved inward during 3 months. Pozzolanic reactions in the samples with 30 mass% of additives depleted portlandite, however, higher amounts of C–(A)–S–H phases with lower C/S ratio, denser microstructure and faster carbonation of surface parts ensured their resistance against carbonation throughout the monitored period.

Keywords Carbonation · Silica fume · Metakaolin · Ground-granulated blast-furnace slag

Abbreviations

A	Al_2O_3
Aft	Ettringite
C	CaO
C–A–H	Calcium aluminate hydrate
C–A–S–H	Calcium alumina silicate hydrate
C–S–H	Calcium silicate hydrate
$\overline{C}$	CO_2
C/S	CaO/SiO_2
F	Fe_2O_3
FTIR	Fourier transform infrared spectroscopy
H	H_2O
IR	Infrared
M	MgO
MIR	Middle infrared spectroscopy
S	SiO_2
SF	Silica fume
$\overline{S}$	SO_3
SO_4-AFm	Monosulfate
TGA	Thermogravimetric analysis
XRD	X-ray diffraction

✉ Eva Kuzielová
eva.kuzielova@stuba.sk

1 Institute of Construction and Architecture, Slovak Academy of Sciences, Dúbravská Cesta 9, 845 03 Bratislava, Slovak Republic

2 Faculty of Chemical and Food Technology, Slovak University of Technology, Radlinského 9, 812 37 Bratislava, Slovak Republic

3 Institute of Inorganic Chemistry, Slovak Academy of Sciences, Dúbravská Cesta 9, 845 36 Bratislava, Slovak Republic

4 Faculty of Chemistry, Materials Research Centre, Brno University of Technology, Purkyňova 118, 612 00 Brno, Czech Republic

Introduction

Carbon dioxide sequestration in cementitious materials includes many different technologies, which are applied to improve their properties as well as to reduce CO_2 footprints by enforced carbonation. Natural carbonation, depending on its extent, does not only have to increase the strength of Portland cement-based materials by refinement of pore structure but, on the contrary, can also weaken the structure and increase the permeability of the material. In applications, where cementitious materials are exposed to elevated CO_2 concentrations, such as wells for oil and gas operations, it is therefore needed to design carbonation-resistant cements.

An underlying mechanism of carbonation can be described as follows. The CO_2 dissolved in the pore solution forms carbonic acid, which causes the decrease in pH of the otherwise highly basic pore solution. This leads to the dissolving of $Ca(OH)_2$(s) mainly and the subsequent formation of $CaCO_3$(s). Leaching of $Ca(OH)_2$ leads to a small increase in porosity, however, the cement degradation will not occur, if the reactions stopped at this stage [1]. On the contrary, formed $CaCO_3$ serves as a less permeable barrier for another acid attack. The decreased porosity and the higher compressive strengths can be reported since calcite has a higher molar volume than portlandite. Present $Ca(OH)_2$ keeps the pH above 12 and dissolved CO_2 is in the form of CO_3^{2-}. However, after the $Ca(OH)_2$ is depleted, $CaCO_3$ starts to dissolve, pH drops below 11, and instead of CO_3^{2-}, HCO_3^- begins to dominate [2]. Water-soluble calcium hydrogencarbonate then forms, which can easily diffuse out of the cement matrix. Change of the pH causes also the decalcification of C–(A)–S–H phases, which are converted to silica-rich C–(A)–S–H and amorphous silica gel. In comparison with portlandite, the much larger reactive surface of C–(A)–S–H precludes the buildup of the resistance by the formation of $CaCO_3$ impermeable layer and reactions continue [3]. Unhydrated clinker phases, alite and belite, are also decalcified at this stage, while C_3A and C_4AF do not react considerably [4–6]. The remaining material is highly porous and weakened. As was proposed in [3, 7], carbonation shrinkage can be caused by the shrinkage of the inner C–S–H region resulting from the loss of Ca^{2+}.

Herterich et al. [3] showed that also AFm phases are involved in the early carbonation reactions, even under ambient conditions, and contribute to the production of carbonates. Before their complete decalcification, they transform to hemi- and monocarboaluminate.

The prevalent carbonation product is calcite as the only stable polymorph of $CaCO_3$, however, also other modifications, vaterite and aragonite, can be present [8, 9]. Besides, the formation of amorphous calcium carbonate is also reported [10]. This phase plays an important role in the carbonation resistance of cements, but its origin is still not well understood. Local concentration of CO_2 [11, 12], pH of the associated solution [13], silicon concentration in the solution coming from C–S–H phases [14, 15], the content of sulfate [9, 16, 17], but mainly water to binder ratio (w/b) belong among the factors influencing crystallinity of $CaCO_3$. Low water content leads to the limited space available for calcium carbonate precipitation, which in turn promotes the formation of metastable forms [18]. Furthermore, while a reduced w/b ratio also leads to decreased porosity and consequently to reduced CO_2 diffusion rates, its higher value ensures encouragement of early-age hydration, leading to increased portlandite contents associated with increasing carbonation resistance [3]. Therefore, some concordance must be found.

The mitigating effect of amorphous calcium carbonate on the carbonation process relates to its higher solubility in comparison with crystalline forms. It maintains a higher calcium concentration in the pore solution and in this way decreases the driving force for decalcification of the C–(A)–S–H. Some studies confirmed the stabilization influence of magnesium on the amorphous calcium carbonate [19, 20]. However, based on the study of alkali-activated slags, McCaslin and White [11] pointed out that the propensity for decalcification is also controlled by the availability of silicate ions in the pore solution. Kellermeier et al. [21] stabilized amorphous calcium carbonate by sodium silicate. They found that growing amorphous calcium carbonate particles caused a local decrease in pH nearby their surface. This led to the polymerization of silica in their vicinity, which in turn arrested the growth of carbonate. The thickness and porosity of these coatings differed based on the silica concentration, thus slowing down the crystallization of amorphous calcium carbonate to a different degree or completely preventing it from being.

In the case of slag containing systems, however, also the formation of hydrotalcite-like phase takes place, which is also known to prevent decalcification and carbonation progress [22, 23]. As Liu et al. [24] demonstrated, its in-situ formation can be promoted by an increased amount of Al^{3+} in the system.

The paper is focused on the evaluation of carbonation progress and resistance of the selected systems against carbonation based on the phase composition evolution. Ternary cement mixtures consisting of class G cement in combination with SF, MK, or BFS as supplementary cementitious materials were designated based on our previous results [25] as potentially suitable for applications in geothermal wells. Compositions were submitted to accelerated carbonation from 1 day up the 1 year. Identification of the formed phases was performed by TGA, XRD, and FTIR.

Materials and methods

High sulfate resistant portland cement Class G (Dyckerhoff GmbH, Germany), metakaolin L_{05} (Mefisto, České lupkové závody a.s., Czech Republic), silica fume (SF; Oravské ferozliatinárske závody, a.s., Slovak Republic), and ground-granulated blast-furnace slag (BFS; Kotouč Štramberk, spol. s r.o., Czech Republic) were used for the preparation of cement pastes with the compositions shown in Table 1. The oxide composition of input materials and their specific surfaces are presented in Table 2. Detailed structural characterization of the used materials by FTIR spectroscopy was reported in [25].

All pastes were prepared with equal water to binder ratio (0.44). In the case of the composite samples, plasticizer

Table 1 Composition (in mass%) and designation of the prepared samples (cement—D, silica fume—SF, metakaolin—MK, blast furnace slag—BFS; the number before the abbreviation of additive indicates its mass percentage in the sample)

Sample	w_{PC}	w_{SF}	w_{MK}	w_{BFS}
D	100	–	–	–
D15SF15MK	70	15	15	–
D15SF15BFS			–	15
D30SF30MK	40	30	30	–
D30SF30BFS			–	30
D7SF23MK	70	7.5	22.5	–

Stachement® 903 (Stachema Bratislava, a.s., Rovinka, Slovakia) was applied to reduce the water demand. The plasticizer was selected following the main purpose of the research focused on the geothermal well conditions. Its concentration (0.5 g per 100 g of the binder) in water was kept constant.

Dry mixtures were homogenized along with the gradual addition of water. After the whole amount of water was added, 6 min of additional homogenization using the cement mixer followed. Three prisms with dimensions of 160 × 40 × 40 mm were prepared from the paste of each composition and for every time.

As the carbonation extension is significantly influenced by the time at which the carbonation is initiated [5, 26], samples were put into a CO_2 chamber immediately after preparation. After one day, samples were demolded, placed again into the chamber, and left there for 1 week, 3, 6, and 12 months including the first day in the molds. Accelerated carbonation was performed using the following test conditions: a CO_2 concentration equal to (20.0 ± 1) vol%, a temperature of (50 ± 1) °C, and relative humidity of (90 ± 2) %.

At the specified times, the prisms were cut and the surface, as well as middle parts of the samples, were ground, dried, and subjected to analyses. Hydration was stopped using acetone, diethyl ether, and pressure filtration. Residual solvents were removed by vacuum drying. It should be noted that in the case of one-day samples, access to CO_2 was possible only from the upper part.

Phase changes occurring in the samples were monitored by the TGA technique (TGA/DSC–1, STARe software 9.30, Mettler Toledo). The 50.00 (± 0.1) mg of powdered samples was heated in the open platinum crucibles for up to 1000 °C at the heating rate of 10 °C min^{-1} in the atmosphere of synthetic air (purity 5.0, 30 mL min^{-1}).

The infrared spectra were performed using Nicolet 6700 FTIR spectrometer from Thermo Scientific™. The IR source, KBr beam splitter, and DTGS detector were used for the mid-IR (MIR) measurements (4000–400 cm^{-1}). MIR transmission spectra were collected using the KBr pellet technique (1 mg of a sample homogenized with 200 mg KBr). KBr pellets were dried for 16 h at 50 °C. For each sample, 64 scans were recorded with a resolution of 4 cm^{-1}. The Thermo Scientific package (OMNIC™ software) was used for the spectra processing and to detect the exact position of the vibrational bands appearing as inflections/shoulders in the IR spectra involving the Savitzky-Golay second derivatives. One should be aware that since the position of the maximum absorption band changed with carbonation curing time, spectra were not normalized.

Crystalline phases in the samples were detected by XRD analysis (Diffractometer system EMPYREAN, PANanalytical, the Netherlands; CuKα radiation, $\lambda = 0.1540598$ nm, operating at 40 kV and 30 mA). The experiments were performed within the values of 2θ ranging from 5° to 90° with an angular step of 2θ equal to 0.013° and 25 s duration, using automatic divergence slits to maintain the constant irradiation of the sample area. The irradiated length was 10 mm.

Results and discussion

FTIR spectroscopy

The absorption spectra of the samples after different times of carbonation are depicted in Figs. 1–7. Infrared spectra in the area of higher wavenumbers for 7-day, 3-month, and 6-month samples are provided in the supplementary material. Above 3600 cm^{-1}, the absorption bands from water and other OH species can be observed. Since both, the stretching vibration of Ca–OH from portlandite and the strong one from ettringite manifest at 3640 cm^{-1} [27], determination of ettringite in this region is difficult. The hump at about 3530 cm^{-1} also belongs to the stretching vibration of Al–OH in the structure of ettringite [28], its

Table 2 Oxide composition, loss of ignition, and specific surface of the used initial materials

	Oxide composition/mass%						Loss of ignition/mass%	Specific surface/ m^2 kg^{-1}	
	CaO	SiO_2	Al_2O_3	Fe_2O_3	MgO	SO_3			
Dyckerhoff	62.73	20.12	4.46	5.05	0.95	2.21	1.70	Blaine	326.5 ± 0.1
SF	0.50	97.10	0.21	–	0.40	–	2.36	BET	15,000
MK	0.24	49.70	42.36	0.79	0.22	0.08	5.39	Blaine	2586 ± 38
BFS	36.53	35.76	9.39	0.24	14.0	0.03	1.53	Blaine	469.9 ± 0.5

Depicted values of a specific surface area represent the average of three measurements

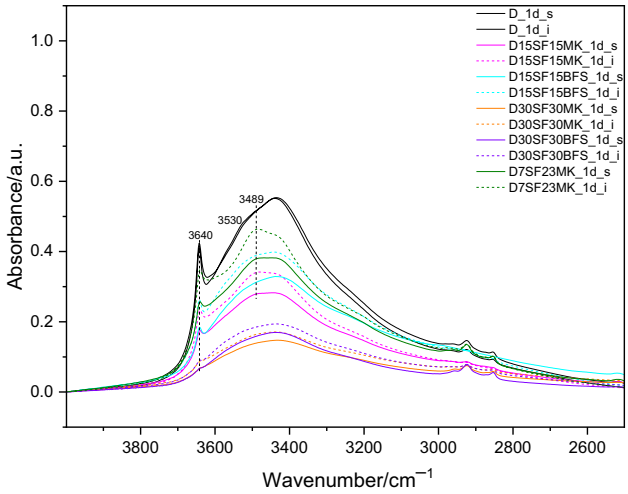

Fig. 1 Segment of infrared spectra of the samples after 1 day of carbonation in the area of OH species stretching vibrations. (Color figure online)

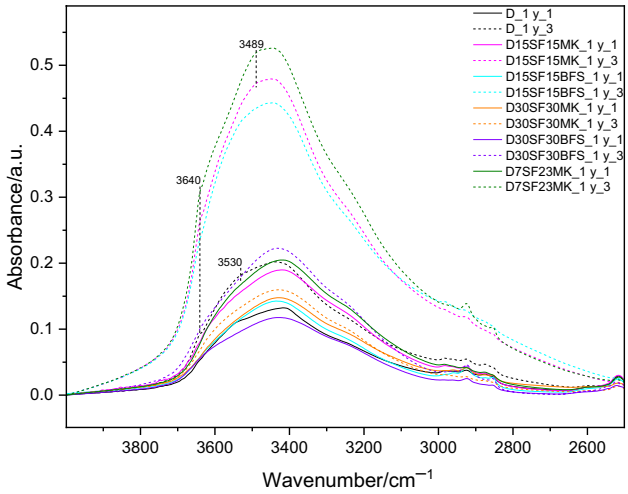

Fig. 2 Segment of infrared spectra of the samples after 1 year of carbonation in the area of OH species stretching vibrations. (Color figure online)

presence is, however, visible only in the case of referential pastes. Instead of this, the hump at 3489 cm^{-1} caused by the presence of SO_4-AFm phase appears in blended compositions [29]. Progressing carbonation caused gradual diminishing of both these bands in accordance with the results of other analyses and changed also the fashion of the absorption band due to corresponding bending vibrations of OH groups (Figs. 1–2). Instead of an ordinary separate band occurring between 1720 and 1580 cm^{-1}, a hump on the dominant band belonging to the stretching vibrations of C=O in CO_3^{2-} is observed, especially in the case of surface areas of the samples (Figs. 3–7).

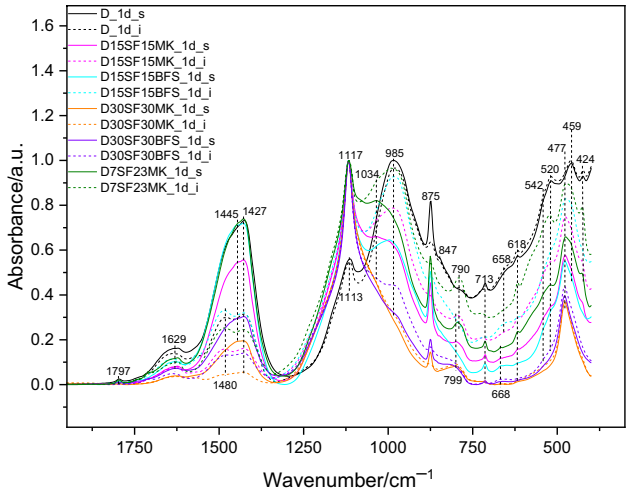

Fig. 3 Segment of infrared spectra of the samples after 1 day of carbonation. The assignment of the band not mentioned in the text: 1034 $cm.^{-1}$—Al–OH bending vibration mainly from SO_4-AFm [63]. (Color figure online)

Although the region of the stretching vibrations of C=O in CO_3^{2-} is difficult to describe due to the overlapping of individual bands coming from different $CaCO_3$ modifications, it changed with progressing carbonation as follows. A double band with the maxima at about 1480 and 1427 cm^{-1} can be observed at the beginning of carbonation (Fig. 3). The first one is probably caused by different degrees of structure disordering in non-crystalline carbonates, the second one is attributed to the asymmetric stretching vibrations of C=O in calcite as the only crystalline carbonate confirmed by XRD in the particular samples [30]. Enhanced carbonation of the surface parts caused already during the first day of carbonation the flattening in the area of the hump at 1480 cm^{-1}, which indicates crystallization of amorphous carbonates. From the time of 7 days, the presence of vaterite and aragonite was evidently detected in the upper parts, which could lead to the appearance of the hump at about 1445 cm^{-1} (Fig. 4). Other analyses and manifestation of bending vibrations in aragonite and vaterite suggest the highest amounts of these phases in the compositions with BFS. The same composition also demonstrates a more significant hump at about 1470 cm^{-1}.

Bending vibrations of O–C–O in CO_3^{2-} coming from different crystalline modifications demonstrate at 875, 857, 744, 713, and 700 cm^{-1}. The first one originates from calcite and it is together with the band at 713 cm^{-1} present as the most intense in all samples regardless of the duration of carbonation curing. The absorption band at 713 cm^{-1} results from the overlapped bands of vaterite and calcite [31, 32]. Also, the band at 744 cm^{-1} is caused by

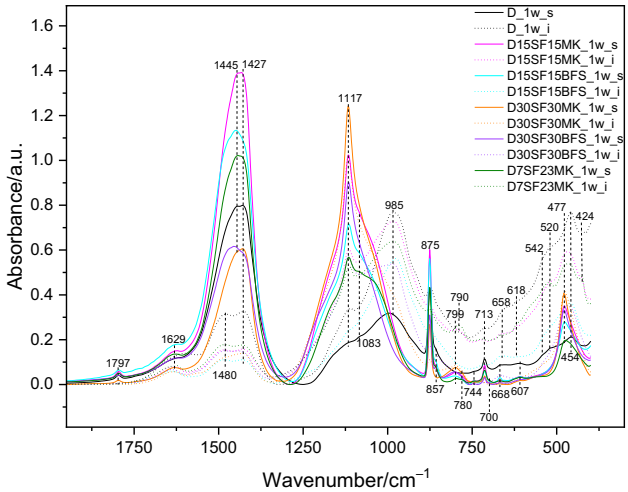

Fig. 4 Segment of infrared spectra of the samples after 1 week of carbonation. (Color figure online)

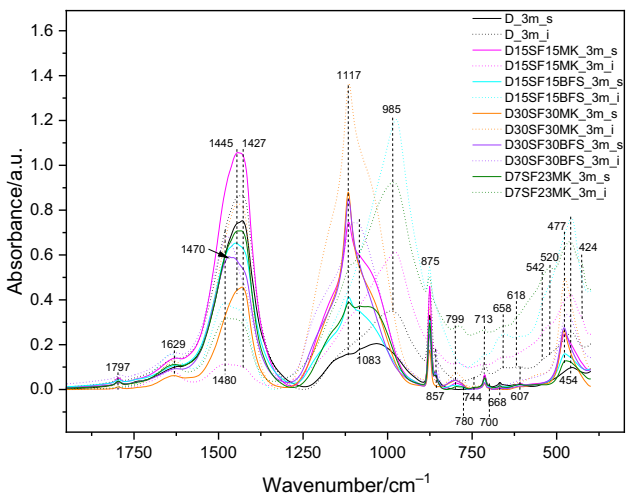

Fig. 5 Segment of infrared spectra of the samples after 3 months of carbonation. (Color figure online)

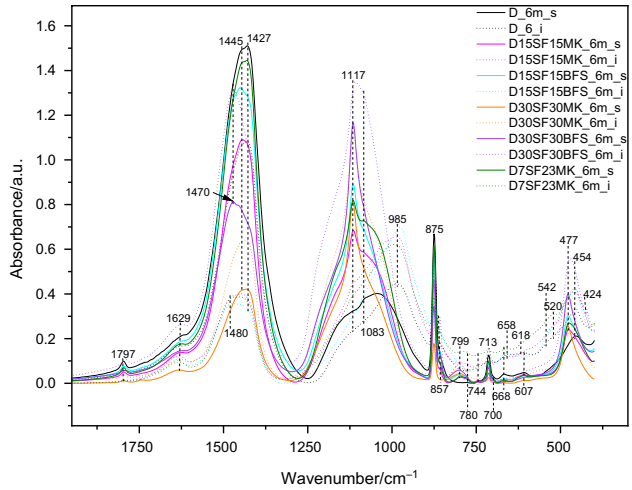

Fig. 6 Segment of infrared spectra of the samples after 6 months of carbonation. (Color figure online)

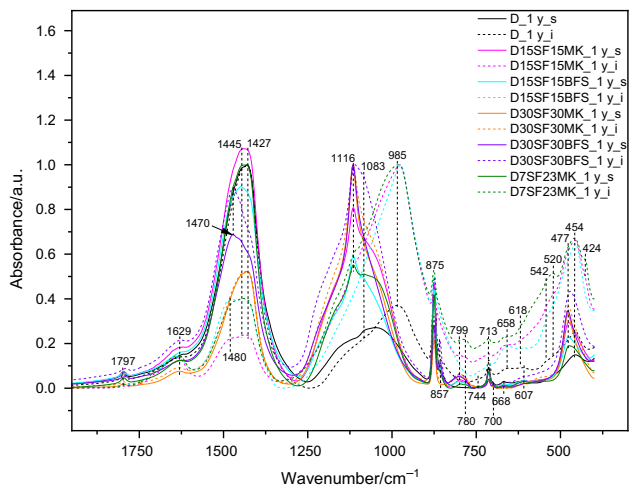

Fig. 7 Segment of infrared spectra of the samples after 1 year of carbonation. (Color figure online)

the presence of vaterite, while those at 857 and 700 cm^{-1} come from the structure of aragonite [33, 34].

Since carbonation of inner parts takes place more slowly, ongoing changes can be better observed. The first changes occurred in the MIR spectra of the samples after 3 months of curing, however, as it was confirmed by other analyses, only in the compositions D, D30SF30MK, and D30SF30BFS (Fig. 5). The hump at 1445 cm^{-1} replaced the one at 1480 cm^{-1}. The same as in the case of the upper part, the hump at 1470 cm^{-1} arose in the spectra of D30SF30BFS. All three compositions contain vaterite based on the demonstration of bending vibrations at 744 cm^{-1}. The absorption bands at 857 and 700 cm^{-1} in the spectra of D30SF30BFS confirm also the presence of aragonite. A slight sign of vaterite can be seen also in D15SF15BFS, however, its certain presence is in all compositions with lower cement replacement level observed only after six months of carbonation (Fig. 6). Its amount did not change after the next six months (Fig. 7). Aragonite was not present even after one year in these samples.

The formation of particular polymorphs of $CaCO_3$ depends on several factors. Besides kinetic factors, carbonation conditions (natural or accelerated carbonation) [35–37], pH, presence of different foreign ions, C/S ratio, and others can cause that in addition to calcite, other polymorphs can be found in the matrix even after a long time [38]. While carbonation of portlandite results in the formation of calcite and vaterite, carbonation of C–(A)–S–H leads to vaterite. Aragonite is formed mainly from ettringite. Both higher pH of pore solution and higher C/S ratio promote vaterite [15,

39, 40], whereas decreased pH and C/S aragonite formation [40–42].

Initial C/S ratios of compositions with MK are lower than those in corresponding compositions prepared with BFS. Besides, some amount of Ca^{2+} is in addition to portlandite and AFt incorporated in the structure of AFm formed in the MK containing compositions. Although the effect of C/S ratio in amorphous hydrates, as well as pH, cannot be excluded without further investigation, preferential formation of aragonite or its higher quantity in the samples with BFS can relate also with higher amount of Mg^{2+} as was proven by Reddy and Nancollas [43]. Higher Mg^{2+} to Ca^{2+} ratios could also lead to the stabilization of amorphous carbonates, which can serve as an inhibitor for progressing carbonation [20]. The results of this study did not lead to the confirmation of such conclusions.

The distinct presence of amorphous calcium carbonate is difficult to confirm due to the overlapping of its stronger vibrations with those from the crystalline carbonates. However, based on the study [44], the weak absorption band around 1797 cm^{-1}, observed in the spectra of upper parts from the beginning of carbonation, comes from the structure of amorphous calcium carbonate. In accordance with other results, spectra of inner parts of referential D show its presence from the time of three months, while the slight indication in blended samples with 30 mass% additives is evident only after six months. The lower intensity of particular band in the spectra of D30SF30MK and D30SF30BFS may be another reason for enhanced carbonation in these samples.

The most significant changes in absorption bands coming from carbonates occurred along with the modification of C–(A)–S–H, AFt, and AFm structure. Stretching vibrations in the silicate units of C_2S exhibited at about 847 cm^{-1} only after 1 day (Fig. 3). Enhanced carbonation caused the movement of the absorption band at about 985 cm^{-1}, assigned to Q^2 silicate species [29, 45], to higher wavenumbers. This, together with the emersion of the wide hump between 1250 and 1130 cm^{-1} and the band at 1083 cm^{-1} [31, 46], indicates the decalcification of C–(A)–S–H and its subsequent polymerization leading to the amorphous silica and alumina gel (Figs. 4–7) [47, 48]. A significant shift happened in the upper parts of all compositions already within the first 7 days. On the contrary, the position remained unchanged till one year of carbonation in the inner parts of compositions D, D15SF15MK, D15SF15BFS, and D7SF23MK (Fig. 7). Among these compositions, the position of Si–O asymmetric stretching vibration generated by Q^2 units in D15SF15BFS is slightly shifted to lower wavenumbers, which reflects the expected formation of C–(A)–S–H with a higher C/S ratio.

Regarding bending vibrations in composition D, the absorption band at 520 cm^{-1} due to O–Si–O out-of-plane bending vibrations from C_3S diminished gradually. This reflects enhanced polymerization due to both, hydration and carbonation, associated with the decrease in the freedom of motion [49]. The reduction of absorption band intensity is much faster in the upper parts undergoing significant carbonation connected with the decalcification of C_3S. The position of the absorption band coming from in-plane vibration in SiO_4 tetrahedra connected to the formation of C–(A)–S–H at 454 cm^{-1} stayed unchanged [50].

The bending vibration region of blended compositions contains also an absorption band at about 477 cm^{-1}, especially from amorphous SiO_2 in SF. Where applicable, also the overlapping with Si–O bending vibration from the structure of MK occurs [25]. The band at 477 cm^{-1} dominates in the spectra of the upper parts regardless of the composition and duration of carbonation. Unlike the referential sample, the out-of-plane bending vibrations did not exhibit at 520 cm^{-1} already after the first day of carbonation (Fig. 4). Decalcification of clinker phases thus took place faster because of the fast depletion of portlandite. The covering of the absorption band due to internal deformation of SiO_4 tetrahedra by that from SF and/or MK points out the restricted hydration and pozzolanic reactions by carbonation. This is further supported by the presence of an absorption band at 799 cm^{-1} also coming from unreacted SF and MK [25].

The situation in the inner parts of blended compositions is different. In the case of D15SF15BFS, the absorption band at about 454 cm^{-1} reached higher intensity than that at 477 cm^{-1} within the first 7 days (Fig. 4), in the spectra of D15SF15MK and D7SF23MK within 3 months (Fig. 5). The position of this band does not seem to be changing with the duration of carbonation. Besides, the longer the time, the more obvious hump centered around 485 cm^{-1} can be observed in the spectra of samples prepared with 15 mass% SF. In [51], the occurrence of this band was attributed to the SiO_4 deformation in the structure of tobermorite (both 1.1. and 1.4 nm tobermorite). On the contrary, in earlier times, the absorption band at approximately 790 cm^{-1} confirms the presence of Q^1 silicate species in C–(A)–S–H. Longer times resulted in its disappearance and in the case of compositions with MK also to the splitting of this band, which may probably reflect a change in the ratio of Q^1 and Q^2 species.

The absorption band positioned at 658 cm^{-1} assigned to O–Si–O bending and H_2O librations [52, 53] is present in the inner parts of referential D and compositions with lower cement replacement level throughout the monitored time. The most pronounced is the particular band in the MIR spectra of D15SF15BFS, which can relate, in accordance with [54], to different C/S ratio in the formed C–(A)–S–H phases but also to the different amount of water in these hydrates [55].

The absorption bands from O–Si–O bending vibrations in C–(A)–S–H cannot be or are difficult to recognize in the spectra of samples with higher cement replacement level.

Because the strong stretching Si–O vibrations from SF (at about 1117 cm^{-1}) overlaps with that of sulfate in the blended samples, carbonation of sulfates can be better observed only in the spectra of referential D composition. At the beginning of carbonation, the asymmetric stretching vibration of S–O in SO_4^{2-} in AFt demonstrates by the band at 1113 cm^{-1} in the upper as well as inner part (Fig. 3) [56, 57]. Bending vibration of Al–(O–H) in AFt overlapping with asymmetric bending vibration of S–O manifests at 618 cm^{-1} [56]. Another asymmetric bending vibration of S–O in AFt occurs at 542 cm^{-1}. The absorption band at 424 cm^{-1} can be assigned to the O–S–O symmetric bending vibration overlapping with that of Al–O–H. Based on our earlier study [29], however, the stronger manifestation of SO_4-AFm occurs at this wavenumber. The disappearance of the absorption band at 424 cm^{-1} before other absorption bands from AFt in the inner parts of the samples together with the study [58] support this finding. In agreement with other analyses, surface parts underwent significant changes of bands from AFt already after the first day, whereas inner parts demonstrate their presence even after 1 year of carbonation (Fig. 7). However, especially the shift of the band initially situated at 618 cm^{-1} to 607 cm^{-1} can be observed. This may reflect the change of ettringite structure due to CO_3^{2-} for SO_4^{2-} ion exchange [59] pointed out also based on the results of XRD. Together with the diminishing of bands assigned to AFt, the absorption bands of gypsum appeared in the spectra. (the asymmetric bending vibrations from SO_4^{2-} tetrahedral at 668 cm^{-1} and 607 cm^{-1}; formation of hump between 1200 and 1100 cm^{-1} due to asymmetric stretching vibration in SO_4^{2-}) [57, 60–62].

Thermal analysis and XRD

Selected XRD patterns and DTG curves of cement pastes carbonated for different times are depicted in Figs. 8–16, respectively. The determined mass losses in the temperature areas corresponding with the decomposition of different phases are shown in Table. 3.

As it is documented by shown XRD patterns (Figs. 8–11), the remnant initial crystalline phases were detected in all carbonated pastes following their composition and degree of hydration: hatrurite, larnite, and brownmillerite from cement, quartz and mullite from MK, and merwinite together with åkermanite-gehlenite solid solution from BFS. Cristobalite was documented in the case of higher substitution level of cement by MK. Concerning hydration products, no other phases than ettringite, SO_4-AFm, and portlandite were confirmed after the carbonation process. The present SO_4-AFm phase is in the form of kuzelite.

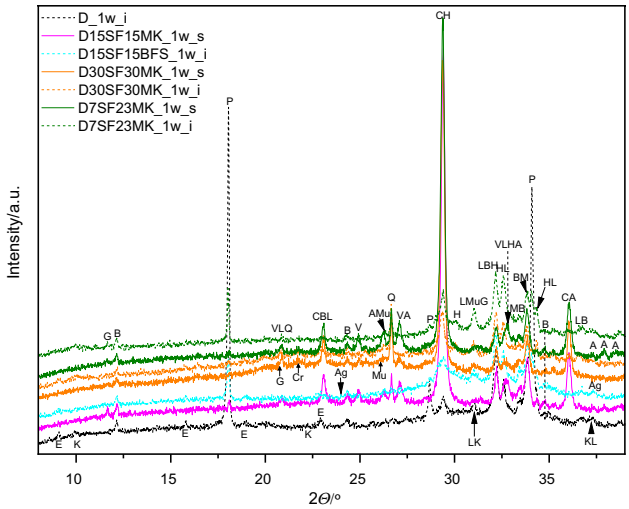

Fig. 8 Segment of XRD patterns of the cement pastes carbonated for 7 days. Abbreviations: A—aragonite ($C\overline{C}$), Ag—åkermanite-gehlenite ($Ca_2Mg(Si_2O_7)$ to $Ca_2Al(AlSiO_7)$), B—brownmillerite ($\underline{C}_4AF$), C—calcite ($C\overline{C}$), Cr—cristobalite (S), E—ettringite ($C_6A_6\ \overline{S}_3H_{32}$), G—gypsum ($C\overline{S}H_2$), H—hatruite ($C_3S$), K—kuzelite-monosulfate ($C_4A\overline{S}H_{12}$), L—larnite (β-C_2S), M—merwinite (MC_3S_2), Mu—mullite (A_3S_2), P—portlandite (CH), Q—quartz (S), V—vaterite ($C\overline{C}$). (Color figure online)

The quantity of C_4AF deduced based on XRD does not show distinct differences that supports the conclusion of several studies [4–6], according to which its carbonation takes place slowly. On the other hand, the intensity of diffractions belonging to β-C_2S and C_3S decreased due to continuing hydration as well as decalcification. An increase in C–(A)–S–H and C–A–H phases with time was based on

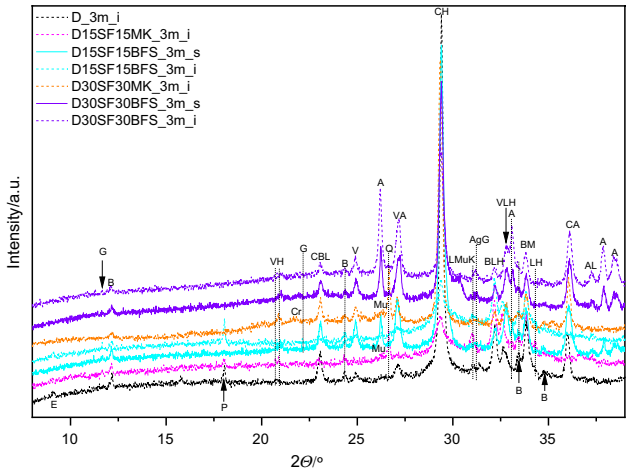

Fig. 9 Segment of XRD patterns of the cement pastes carbonated for 3 months. (Color figure online)

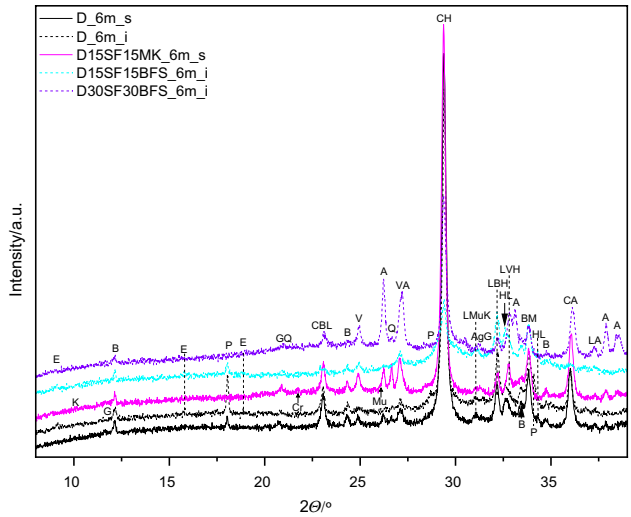

Fig. 10 Segment of XRD patterns of the cement pastes carbonated for 6 months. (Color figure online)

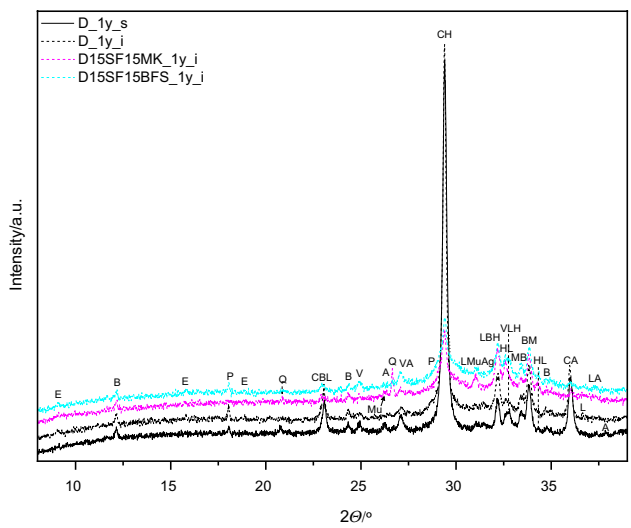

Fig. 11 Segment of XRD patterns of the cement pastes carbonated for 1 year. (Color figure online)

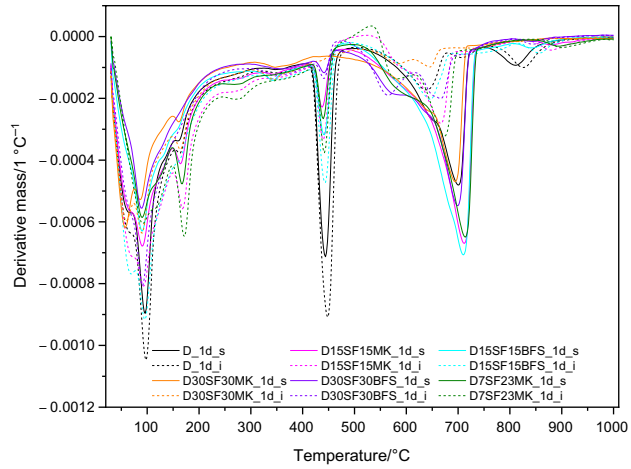

Fig. 12 DTG curves of the samples after one day of carbonation. (Color figure online)

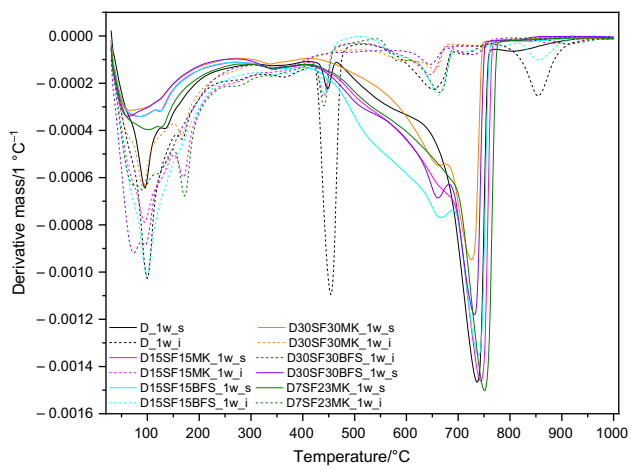

Fig. 13 DTG curves of the samples after one week of carbonation. (Color figure online)

DTG confirmed only in the inner parts of blended compositions with a lower replacement level of cement (Tab. 3). Ongoing hydration of inner parts also showed D composition, however, amount of hydration products did not rise continuously. In the case of all surface parts as well as other compositions, the results point out that carbonation rate is distinctly higher than hydration and/or pozzolanic reactions rate.

In accordance with the results of FTIR, the most rapid carbonation of the surface parts took place already within the first 7 days. No big differences were determined from this time up to the monitored one year. Considering inner parts of unblended cement paste and compositions with higher substitution level of cement, the most significant changes were recorded between the first 7 days and 3 months. In the case of blended compositions, the reason for progressing carbonation deeper into the samples relates to the missing buffering effect of portlandite, which was due to the high quantity of additives consumed even before the first 7 days of curing.

Since in unblended cement paste the portlandite was in both the outer and inner parts still detected after 6 months and ongoing hydration was confirmed also by a small increase in.

C–(A)–S–H as well as portlandite amount from 3 to 6 months, the advance of carbonation can be associated with the pore structure of the carbonated surface area, which did not avoid the diffusion of CO_2 deeper as well as with

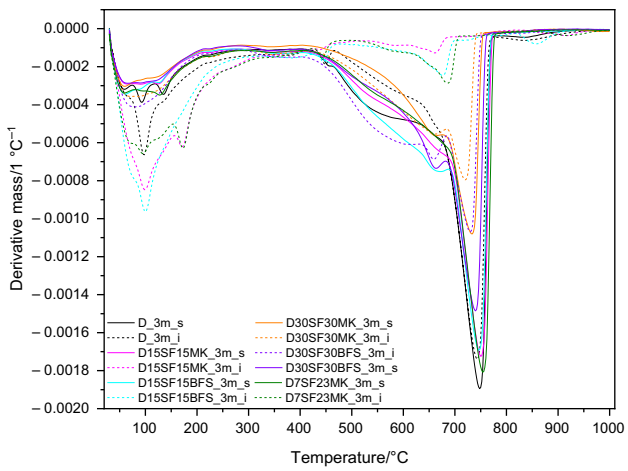

Fig. 14 DTG curves of the samples after three months of carbonation. (Color figure online)

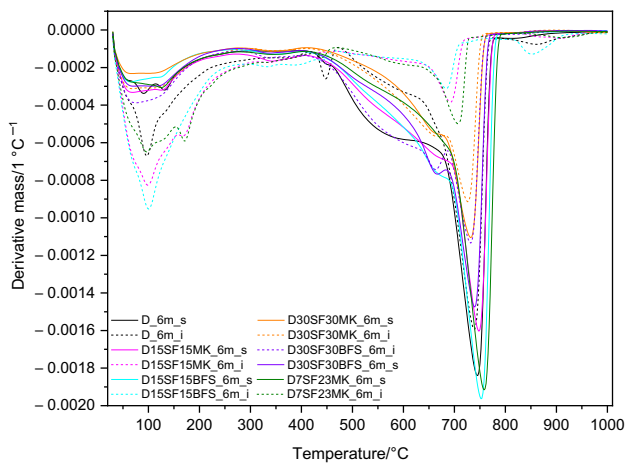

Fig. 15 DTG curves of the samples after six months of carbonation. (Color figure online)

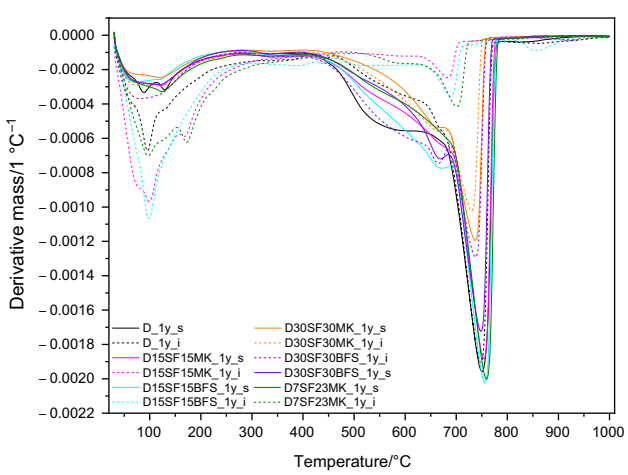

Fig. 16 DTG curves of the samples after one year of carbonation. (Color figure online)

composition of pore solution and its quantity in available pores as necessary medium and one of the reactants during carbonation reactions.

On the contrary, a lower replacement level of cement in the total amount of 30 mass% seems to successfully prevent considerable carbonation of inner parts. XRD diffractions of β-C_2S and C_3S clinker phases in these samples do not show significant differences at different times and the detected quantity of carbonates is low. In general, the lowest amount of carbonates was detected in D15SF15MK composition, followed by D15SF15BFS and D7SF23MK, although portlandite was depleted in the surface area of all these samples already within the first 7 days. In the inner parts, its detectable amounts were still present in the compositions of one-year D15SF15BFS and D7SF23MK samples, while the composition D15SF15MK did not show its traces after 3 months of curing based on TGA. Even though, the determined amounts of.

C–(A)–S–H phases in the inner parts of all these compositions increased with time and reached even higher values than corresponding ones in the referential D pastes. This points out that, unlike upper parts, portlandite was preferentially consumed in pozzolanic reactions and did not participate in carbonation reactions significantly.

Besides carbonation of portlandite and C–(A)–S–H phases, carbonation of ettringite and.

SO_4-AFm phases can be observed. Moreover, the decreased mass losses in the area of C–A–H decomposition temperatures indicate also the carbonation of these phases. In the upper parts of the samples, reformation of gypsum from Aft manifesting as DTG peak at approximately 130 °C occurred already within the first 7 days regardless of the composition. In the inner parts, ettringite degradation strongly depended on the particular composition and progress of carbonation. XRD confirmed its presence accompanied by portlandite in D and compositions with a lower substitution level of cement even after 1 year. Its gradual transformation before complete decomposition can be, however, observed by the shift of its diffraction maxima, change of shape, and appearance of gypsum.

The presence of monosulfate, determined based on the DTG peak around 160–170 °C, clearly reflects the initial composition of the samples, and the degree of hydration, both affecting time of sulfate ions depletion, and simultaneous carbonation. The highest amount of this phase shows D7SF23MK composition followed by D15SF15MK, while in the D30SF30BFS this phase was not detected at all. As in the case of ettringite, the analysis of the surface areas confirmed SO_4-AFm only in the 1-day samples (Fig. 12). This indicates that the carbonation of this phase started immediately upon exposure to CO_2. In the inner parts of D and D30SF30MK compositions, monosulfate is no longer detected from the time of 3 months (Fig. 14). On

Table 3 Total mass loss and mass loss of carbonated cement pastes in different temperature intervals corresponding with particular hydration products

Sample	Carbonation time	Part of sample	Temperature interval/°C			
			r.t.–400 (C(–A)–S–H, C–A–H)	400–500 (CH)	500–1000 (carbonates)	Total mass loss/%
D	1 day	s	10.1	2.2	5.0	17.3
		i	11.4	3.0	2.9	17.3
	7 days	s	8.6	0.8	15.2	24.6
		i	12.4	3.5	4.3	20.2
	3 months	s	6.9	0.8	20.9	28.6
		i	9.3	0.6	17.4	27.3
	6 months	s	6.9	0.6	22.8	30.3
		i	10.3	0.8	16.3	27.4
	1 year	s	6.2	–	24.4	30.6
		i	10.1	0.4	18.7	29.2
D15SF15MK	1 day	s	10.1	0.7	6.5	17.3
		i	12.5	0.9	2.8	16.2
	7 days	s	7.0	–	18.2	25.2
		i	13.0	0.9	2.2	16.1
	3 months	s	6.4	–	20.3	26.7
		i	13.8	0.7	2.2	16.7
	6 months	s	7.6	–	20.6	28.2
		i	14.7	–	5.3	20.0
	1 year	s	6.3	–	21.1	27.4
		i	14.6	–	4.5	19.1
D15SF15BFS	1 day	s	8.6	0.9	6.9	16.4
		i	12.1	1.4	2.8	16.3
	7 days	s	6.8	–	20.3	27.1
		i	13.8	0.7	3.2	17.7
	3 months	s	6.6	–	22.1	28.7
		i	13.8	0.6	3.9	18.3
	6 months	s	6.0	–	23.4	29.4
		i	14.8	0.5	5.6	20.9
	1 year	s	5.7	–	23.8	29.5
		i	14.2	0.5	6.0	20.7
D30SF30MK	1 day	s	8.2	0.2	5.0	13.4
		i	9.7	0.5	1.7	11.9
	7 days	s	6.2	+	12.2	18.4
		i	10.5	–	2.2	12.7
	3 months	s	5.8	+	13.3	19.1
		i	7.4	–	12.6	20.0
	6 months	s	5.5	–	13.5	19.0
		i	6.8	–	12.9	19.7
	1 year	s	5.3	–	13.5	18.8
		i	6.3	–	13.2	19.5

Table 3 (continued)

Sample	Carbonation time	Part of sample	Temperature interval/°C			
			r.t.–400 (C(–A)–S–H, C–A–H)	400–500 (CH)	500–1000 (carbonates)	Total mass loss/%
D30SF30BFS	1 day	s	7.4	0.4	5.6	13.4
		i	9.9	0.4	3.2	13.5
	7 days	s	6.5	–	15.9	22.4
		i	13.3	–	2.3	15.6
	3 months	s	5.9	–	18.2	24.1
		i	7.7	–	18.2	25.9
	6 months	s	6.4	–	18.8	25.2
		i	7.6	–	18.8	26.4
	1 year	s	5.8	–	19.3	25.1
		i	7.1	–	19.3	26.3
D7SF23MK	1 day	s	9.5	0.7	6.3	16.5
		i	11.2	0.9	3.1	15.2
	7 days	s	7.9	–	18.0	25.9
		i	13.1	1.0	2.6	16.7
	3 months	s	7.3	–	20.2	27.5
		i	13.0	0.6	3.7	17.3
	6 months	s	6.7	–	20.7	27.4
		i	13.0	0.5	6.1	19.6
	1 year	s	6.7	–	21.0	27.7
		I4	13.2	0.6	5.1	18.9

Displayed temperature intervals are only approximate. Corresponding mass losses were determined according to the particular DTG curves. Abbreviated part of sample: s—surface, i—inner part

the contrary, inner parts of D7SF23MK and D15SF15MK demonstrate its presence even after 1 year of carbonation curing which relates to its higher content in these compositions, however, also to the reduced progress of carbonation into the depth of the samples (Fig. 16). The formation of hemicarboaluminate and monocarboaluminate that should precede complete decomposition of AFm was not clearly observed. In addition to that, the formation of poorly crystalline phases can be supposed, an overlapping of maximum diffraction peak of gypsum with that of monocarboaluminate is possible based on the literature [64].

The mentioned results suggest that especially the stability of AFm is sensitive to both, the drop in pH but also to the presence of carbonates. Rothstein et al. [65] demonstrated that even small carbonate contents shift the stability of sulfate-rich AFm to higher pH and high carbonate dosages cause their destabilization over the entire pH range relevant to Portland cement systems. On the contrary, the addition of carbonates increases the mass fraction of AFt, especially at lower pH [66–68].

At the same times, when a significant drop in portlandite amount resulted in the formation of gypsum and the disappearance of SO_4-AFm, a wide-spread mass loss between approximately 500 and 650 °C emerges, which can be attributed to the decomposition of amorphous carbonate as well as less stable modifications of $CaCO_3$, vaterite, and aragonite [31, 69]. Except for referential composition and compositions with higher cement replacement level, which underwent also significant carbonation of inner parts at later times, this wide shoulder appears only on the DTG curves of surfaces. The less thermal stable carbonates thus clearly form by carbonation of C–(A)–S–H phases, AFt, AFm, and clinker phases. A higher amount of vaterite and aragonite resulted in the formation of a distinct DTG peak with the maximum at about 660 °C. In addition to the main carbonate peak spreading between 700 and 760 °C and assigned to calcite, small mass losses are detected above 800 °C in some samples. Some authors attributed them to the decomposition of CO_3-AFm.

According to the XRD, calcite, the dominant carbonation product, was present from the beginning of

carbonation (Fig. 8). In line with the results of thermal analyses, it was the only crystalline carbonate till the time when portlandite was totally consumed or its amount was significantly decreased. Consequently, vaterite and aragonite appeared as a result of other hydration products and clinker phases decalcification first in the surface area of the samples already from the time of 7 days (Fig. 8). Although their transformation to more stable calcite can be expected, they are still present in the upper parts of 1-year samples (Fig. 11). In the inner parts, they were detected in the 3-month D, D30SF30MK, and D30SF30BFS (Fig. 9). Both these phases appeared already in the times when ettringite was still present in the systems. The diffractions of vaterite occurred in compositions with 30 mass% of additives after 6 months (Fig. 10), but were very small even after 1 year of carbonation.

When XRD patterns of inner parts after 6 months and 1 year (Figs. 10, 11) of carbonation are compared, it can be observed that while the amounts of crystalline metastable carbonates do not differ significantly in D, D15SF15MK, and D15SF15BFS, carbonated D samples demonstrate the substantially higher quantity of calcite. This reflects higher amounts of formed portlandite that was not depleted in pozzolanic reactions. Besides, higher carbonation rate of.

C–(A)–S–H with higher C/S ratio could be expected due to their faster dissolution [70–74].

Conclusions

The study aimed to evaluate the impact of additives (SF-MK and SF-BFS combinations) on the phase evolution and carbonation resistance of blended cement pastes submitted to accelerated carbonation for one year. The obtained results led to the deduction of the following findings.

- Calcite presented the prevalent crystalline carbonate regardless of the duration of carbonation. It was detected together with amorphous calcium carbonate in the surface parts from the beginning of carbonation.
- Both aragonite and vaterite appeared in the outer parts from 7 days till the monitored 1 year. Their occurrence relates to the decalcification of C–(A)–S–H phases, carbonation of sulfates as well as decalcification of C_3S and C_2S leading also to the formation of silica and alumina gel and reformation of gypsum. The inclination of monosulfate to carbonation is higher than that of ettringite. The carbonation of C_4AF was slow.
- The low amount of portlandite, ensuring buffering effect, in the samples with higher cement replacement level (60 mass%) resulted in the enhanced carbonation throughout the cross-section of the samples already during the first 3 months. Hydration and pozzolanic reactions were inhibited by enhanced carbonation.
- Portlandite was in the inner part of referential cement paste still detected after 1 year, in the surface part after 6 months. Even though, the carbonation proceeded inside the samples during 3 months.
- Inner parts of the compositions with 30 mass% of additives did not exhibit signs of significant carbonation even after 1 year. The amount of portlandite in these samples decreased when compared with corresponding unblended cement pastes. The part of portlandite was, however, depleted in the pozzolanic reactions. These led to the formation of additional C–(A)–S–H phases and to the denser microstructure. The expected lower C/S ratio of these amorphous hydrates could contribute to improved resistance against carbonation. Another reason for better resistance of these compositions can be faster carbonation of their surface parts which led to the formation of a less permeable layer.

The investigation of pore structure characteristics and elemental composition of the formed hydrates playing an important role in the progress of carbonation will be the objective of the further research.

Supplementary Information The online version contains supplementary material available at https://doi.org/10.1007/s10973-023-12378-9.

Acknowledgements This work was supported by the courtesy of Slovak Research and Development Agency APVV-19-0490, Slovak Grant Agency VEGA 2/0032/21, and The Czech Science Foundation GA19-16646S.

Author contributions EK contributed to conceptualization, writing, funding acquisition, and supervision. EK, MŽ, MS, and JM helped in methodology, formal analysis, and investigation.

Funding Open access funding provided by The Ministry of Education, Science, Research and Sport of the Slovak Republic in cooperation with Centre for Scientific and Technical Information of the Slovak Republic.

References

1. Teodoriu C, Bello O. A review of cement testing apparatus and methods under CO_2 environment and their impact on well integrity prediction–Where do we stand? J Pet Sci Eng. 2020. https://doi.org/10.1016/j.petrol.2019.106736.
2. Bruckdorfer RA. Carbon dioxide corrosion in oilwell cement. In: SPE Rocky mountain regional meeting. 1986. https://doi.org/10.2118/15176-MS. Accessed 19 May 1986.
3. Herterich J, Richardson I, Moro F, Marchi M, Black L. Microstructure and phase assemblage of low-clinker cements during the early stages of carbonation. Cem Concr Res. 2022. https://doi.org/10.1016/j.cemconres.2021.106643.
4. Zajac M, Lechevallier A, Durdzinski P, et al. CO_2 mineralisation of Portland cement: towards understanding the mechanisms of enforced carbonation. J CO2 Util. 2020. https://doi.org/10.1016/j.jcou.2020.02.015.
5. Zhang D, Ghouleh Z, Shao Y. Review on carbonation curing of cement-based materials. J CO2 Util. 2017. https://doi.org/10.1016/j.jcou.2017.07.003.
6. Liu Z, Meng W. Fundamental understanding of carbonation curing and durability of carbonation-cured cement-based composites: a review. J CO2 Util. 2021. https://doi.org/10.1016/j.jcou.2020.101428.
7. Groves GW, Rodway DI, Richardson IG. The carbonation of hardened cement pastes. Adv Cem Res. 1990. https://doi.org/10.1680/adcr.1990.3.11.117.
8. Kutchko BG, Strazisar BR, Huerta N, et al. CO_2 reaction with hydrated class H well cement under geologic sequestration conditions: effects of flyash admixtures. Environ Sci Technol. 2009. https://doi.org/10.1021/es803007e.
9. Zajac M, Irbe L, Bullerjahn F, et al. Mechanisms of carbonation hydration hardening in Portland cements. Cem Concr Res. 2022. https://doi.org/10.1016/j.cemconres.2021.106687.
10. Liu M, Hong S, Wang Y, et al. Compositions and microstructures of hardened cement paste with carbonation curing and further water curing. Constr Build Mater. 2021. https://doi.org/10.1016/j.conbuildmat.2020.121724.
11. McCaslin ER, White CE. A parametric study of accelerated carbonation in alkali-activated slag. Cem Concr Res. 2021. https://doi.org/10.1016/j.cemconres.2021.106454.
12. Chen T, Gao X. Effect of carbonation curing regime on strength and microstructure of Portland cement paste. J CO2 Util. 2019. https://doi.org/10.1016/j.jcou.2019.05.034.
13. Morandeau A, Thiery M, Dangla P. Investigation of the carbonation mechanism of CH and C-S-H in terms of kinetics, microstructure changes and moisture properties. Cem Concr Res. 2014. https://doi.org/10.1016/j.cemconres.2013.11.015.
14. Ashraf W, Olek J. Elucidating the accelerated carbonation products of calcium silicates using multi-technique approach. J CO2 Util. 2018. https://doi.org/10.1016/j.jcou.2017.11.003.
15. Kellermeier M, Glaab F, Klein R, Melero-García E, Kunzb W, García-Ruiz JM. The effect of silica on polymorphic precipitation of calcium carbonate: an on-line energy-dispersive X-ray diffraction (EDXRD) study. Nanoscale. 2013. https://doi.org/10.1039/C3NR00301A.
16. Flaathen TK, Oelkers EH, Gislason SR, et al. The effect of dissolved sulphate on calcite precipitation kinetics and consequences for subsurface CO_2 storage. Energy Proced. 2011. https://doi.org/10.1016/j.egypro.2011.02.476.
17. Cuesta Mayorga I, Astilleros JM, Fernández-Díaz L. Precipitation of $CaCO_3$ polymorphs from aqueous solutions: the role of pH and sulphate groups. Minerals. 2019. https://doi.org/10.3390/min9030178.
18. Ogino T, Suzuki T, Sawada K. The formation and transformation mechanism of calcium carbonate in water. Geochim Cosmochim Acta. 1987. https://doi.org/10.1016/0016-7037(87)90155-4.
19. Radha AV, Fernandez-Martinez A, Hu Y, et al. Energetic and structural studies of amorphous $Ca_{1-x}Mg_xCO_3{\cdot}nH_2O$ ($0 \leqslant x \leqslant 1$). Geochim Cosmochim Acta. 2012. https://doi.org/10.1016/j.gca.2012.04.056.
20. Loste E, Wilson RM, Seshadri R, et al. The role of magnesium in stabilising amorphous calcium carbonate and controlling calcite morphologies. J Cryst Growth. 2003. https://doi.org/10.1016/S0022-0248(03)01153-9.
21. Kellermeier M, Melero-Garcia E, Glaab F, et al. Stabilization of amorphous calcium carbonate in inorganic silica-rich environments. J Am Chem Soc. 2010. https://doi.org/10.1021/ja106959p.
22. Haha MB, Le Saout G, Winnefeld F, et al. Influence of activator type on hydration kinetics, hydrate assemblage and microstructural development of alkali activated blast-furnace slags. Cem Concr Res. 2011. https://doi.org/10.1016/j.cemconres.2010.11.016.
23. Bernal SA, San Nicolas R, Myers RJ, et al. MgO content of slag controls phase evolution and structural changes induced by accelerated carbonation in alkali-activated binders. Cem Concr Res. 2014. https://doi.org/10.1016/j.cemconres.2013.12.003.
24. Liu T, Yu Q, Brouwers HJH. In-situ formation of layered double hydroxides (LDHs) in sodium aluminate activated slag: the role of Al–O tetrahedra. Cem Concr Res. 2022. https://doi.org/10.1016/j.cemconres.2021.106697.
25. Kuzielová E, Slaný M, Žemlička M, et al. Thermal stability of the phases developed at high-pressure hydrothermal curing of class G cement with different pozzolanic and latent hydraulic additives. J Therm Anal Calorim. 2022. https://doi.org/10.1007/s10973-022-11254-2.
26. Zhang D, Li VC, Ellis BR. Optimal pre-hydration age for CO_2 sequestration through portland cement carbonation. ACS Sustain Chem Eng. 2018. https://doi.org/10.1021/acssuschemeng.8b03699.
27. Bensted J, Varma SP. Some applications of infrared and Raman spectroscopy in cement chemistry. Part 3-hydration of Portland cement and its constituents. Cem Technol. 1974;5(5):440–5.
28. Gastaldi D, Canonico F, Boccaleri E. Ettringite and calcium sulfoaluminate cement: investigation of water content by near-infrared spectroscopy. J Mater Sci. 2009. https://doi.org/10.1007/s10853-009-3812-1.
29. Kuzielová E, Tatarko M, Slaný M, et al. Early and middle stages of multicomponent cement hydration under the effect of geothermal water and increased temperatures. Geothermics. 2023. https://doi.org/10.1016/j.geothermics.2022.102632.
30. Li N, Farzadnia N, Shi C. Microstructural changes in alkali-activated slag mortars induced by accelerated carbonation. Cem Concr Res. 2017. https://doi.org/10.1016/j.cemconres.2017.07.008.
31. Shi Z, Shi C, Wan S, et al. Effect of alkali dosage and silicate modulus on carbonation of alkali-activated slag mortars. Cem Concr Res. 2018. https://doi.org/10.1016/j.cemconres.2018.07.005.
32. Sato M, Matsuda S. Structure of vaterite and infrared spectra. Z Krist. 1969. https://doi.org/10.1524/zkri.1969.129.5-6.405.
33. Ni M, Ratner BD. Differentiating calcium carbonate polymorphs by surface analysis techniques—an XPS and TOF-SIMS study. Surf Interface Anal. 2008. https://doi.org/10.1002/sia.2904.
34. Balmain J, Hannoyer B, Lopez E. Fourier transform infrared spectroscopy (FTIR) and x-ray diffraction analyses of mineral and organic matrix during heating of mother of pearl (nacre) from the shell of the mollusc Pinctada maxima. J Biomed Mater Res. 1999. https://doi.org/10.1002/(SICI)1097-4636(1999)48:5%3C749::AID-JBM22%3E3.0.CO;2-P.

35. Auroy M, Poyet S, Le Bescop P, et al. Comparison between natural and accelerated carbonation (3% CO_2): impact on mineralogy, microstructure, water retention and cracking. Cem Concr Res. 2018. https://doi.org/10.1016/j.cemconres.2018.04.012.
36. Anstice DJ, Page CL, Page MM. The pore solution phase of carbonated cement pastes. Cem Concr Res. 2005. https://doi.org/10.1016/j.cemconres.2004.06.041.
37. Šauman Z. Carbonization of porous concrete and its main binding components. Cem Concr Res. 1971. https://doi.org/10.1016/0008-8846(71)90019-6.
38. Fernández-Díaz L, Fernández-González Á, Prieto M. The role of sulfate groups in controlling $CaCO_3$ polymorphism. Geochim Cosmochim Acta. 2010. https://doi.org/10.1016/j.gca.2010.08.010.
39. Black L, Breen C, Yarwood J, et al. Structural features of C–S–H (I) and its carbonation in air—a Raman spectroscopic study. Part II: carbonated phases. J Am Ceram Soc. 2007. https://doi.org/10.1111/j.1551-2916.2006.01429.x.
40. Kitano Y, Okumura M, Idogaki M. Behavior of dissolved silica in parent solution at the formation of calcium carbonate. Geochem J. 1979. https://doi.org/10.2343/geochemj.13.253.
41. Imai H, Terada T, Miura T, et al. Self-organized formation of porous aragonite with silicate. J Cryst Growth. 2002. https://doi.org/10.1016/S0022-0248(02)01616-0.
42. Kotachi A, Miura T, Imai H. Formation of planar aragonite-type carbonate crystals consisting of iso-oriented subunits. Cryst Growth Des. 2004. https://doi.org/10.1021/cg034257v.
43. Reddy MM, Nancollas GH. The crystallization of calcium carbonate: IV. The effect of magnesium, strontium and sulfate ions. J Cryst Growth. 1976. https://doi.org/10.1016/0022-0248(76)90240-2.
44. Andersen FA, Brečević L. Infrared spectra of amorphous and crystalline calcium carbonate. Acta Chem Scand. 1991. https://doi.org/10.3891/acta.chem.scand.45-1018.
45. Higl J, Hinder D, Rathgeber C, et al. Detailed *in situ* ATR-FTIR spectroscopy study of the early stages of C–S–H formation during hydration of monoclinic C_3S. Cem Concr Res. 2021. https://doi.org/10.1016/j.cemconres.2021.106367.
46. García-Lodeiro I, Fernández-Jiménez A, Blanco MT, et al. FTIR study of the sol–gel synthesis of cementitious gels: C–S–H and N–A–S–H. J Sol–Gel Sci Technol. 2008. https://doi.org/10.1007/s10971-007-1643-6.
47. Shen P, Sun Y, Liu S, et al. Synthesis of amorphous nano-silica from recycled concrete fines by two-step wet carbonation. Cem Concr Res. 2021. https://doi.org/10.1016/j.cemconres.2021.106526.
48. Wu B, Ye G. Carbonation mechanism of different kind of C–S–H: rate and products. In: Jensen OM, Kovler K, De Belie N, editors. Proceedings of the international RILEM conference on materials, systems and structures in civil engineering 2016: segment on concrete with supplementary cementitious materials. Paris: RILEM Publications SARL; 2016. p. 263–72.
49. Yousuf M, Mollah A, Hess TR, et al. An FTIR and XPS investigations of the effects of carbonation on the solidification/stabilization of cement based systems-Portland type V with zinc. Cem Concr Res. 1993. https://doi.org/10.1016/0008-8846(93)90031-4.
50. Del Bosque IS, Martínez-Ramírez S, Blanco-Varela MT. FTIR study of the effect of temperature and nanosilica on the nano structure of C–S–H gel formed by hydrating tricalcium silicate. Constr Build Mater. 2014. https://doi.org/10.1016/j.conbuildmat.2013.10.056.
51. Yu P, Kirkpatrick RJ, Poe B, et al. Structure of calcium silicate hydrate (C–S–H): near-, mid-, and far-infrared spectroscopy. J Am Ceram Soc. 1999. https://doi.org/10.1111/j.1151-2916.1999.tb01826.x.
52. Ylmén R, Jäglid U, Steenari BM, et al. Early hydration and setting of Portland cement monitored by IR, SEM and Vicat techniques. Cem Concr Res. 2009. https://doi.org/10.1016/j.cemconres.2009.01.017.
53. Mollah MY, Kesmez M, Cocke DL. An X-ray diffraction (XRD) and Fourier transform infrared spectroscopic (FT-IR) investigation of the long-term effect on the solidification/stabilization (S/S) of arsenic (V) in Portland cement type-V. Sci Total Environ. 2004. https://doi.org/10.1016/j.scitotenv.2003.09.012.
54. Vidmer A, Sclauzero G, Pasquarello A. Infrared spectra of jennite and tobermorite from first-principles. Cem Concr Res. 2014. https://doi.org/10.1016/j.cemconres.2014.03.004.
55. Yan Y, Yang SY, Miron GD, et al. Effect of alkali hydroxide on calcium silicate hydrate (C–S–H). Cem Concr Res. 2022. https://doi.org/10.1016/j.cemconres.2021.106636.
56. Scholtzová E, Kucková L, Kožíšek J, et al. Structural and spectroscopic characterization of ettringite mineral–combined DFT and experimental study. J Mol Struct. 2015. https://doi.org/10.1016/j.molstruc.2015.06.075.
57. Myneni SCB, Traina SJ, Waychunas GA, et al. Vibrational spectroscopy of functional group chemistry and arsenate coordination in ettringite. Geochim Cosmochim Acta. 1998. https://doi.org/10.1016/S0016-7037(98)00221-X.
58. Trezza MA, Lavat AE. Analysis of the system $3CaO{\cdot}Al_2O_3$–$CaSO_4{\cdot}2H_2O$–$CaCO_3$–H_2O by FT-IR spectroscopy. Cem Concr Res. 2001. https://doi.org/10.1016/S0008-8846(01)00502-6.
59. Zhang L, Glasser FP. Investigation of the microstructure and carbonation of $CS^{-}A$-based concretes removed from service. Cem Concr Res. 2005. https://doi.org/10.1016/j.cemconres.2004.08.007.
60. Wang S, Zhang D, Ma X, et al. Spectroscopic and DFT study on the species and local structure of arsenate incorporated in gypsum lattice. Chem Geol. 2017. https://doi.org/10.1016/j.chemgeo.2017.04.011.
61. Liu Y. Raman, Mid-IR, and NIR spectroscopic study of calcium sulfates and mapping gypsum abundances in Columbus crater. Mars Planet Space Sci. 2018. https://doi.org/10.1016/j.pss.2018.04.010.
62. Seidl V, Knop O, Falk M. Infrared studies of water in crystalline hydrates: gypsum, $CaSO_4{\cdot}2H_2O$. Can J Chem. 1969. https://doi.org/10.1139/v69-223.
63. Djebaili K, Mekhalif Z, Boumaza A, et al. XPS, FTIR, EDX, and XRD analysis of Al_2O_3 scales grown on PM2000 alloy. J Spectrosc. 2015. https://doi.org/10.1155/2015/868109.
64. Wang X, Ni W, Li J, et al. Carbonation of steel slag and gypsum for building materials and associated reaction mechanisms. Cem Concr Res. 2019. https://doi.org/10.1016/j.cemconres.2019.105893.
65. Rothstein D, Thomas JJ, Christensen BJ, et al. Solubility behavior of Ca-, S-, Al-, and Si-bearing solid phases in Portland cement pore solutions as a function of hydration time. Cem Concr Res. 2002. https://doi.org/10.1016/S0008-8846(02)00855-4.
66. Damidot D, Lothenbach B, Herfort D, et al. Thermodynamics and cement science. Cem Concr Res. 2011. https://doi.org/10.1016/j.cemconres.2011.03.018.
67. Zhou Q, Glasser FP. Kinetics and mechanism of the carbonation of ettringite. Adv Cem Res. 2000. https://doi.org/10.1680/adcr.2000.12.3.131.
68. Pajares I, Martínez-Ramírez S, Blanco-Varela MT. Evolution of ettringite in presence of carbonate and silicate ions. Cem Concr Compos. 2003. https://doi.org/10.1016/S0958-9465(03)00113-6.
69. Thiery M, Villain G, Dangla P, et al. Investigation of the carbonation front shape on cementitious materials: effects of the chemical kinetics. Cem Concr Res. 2007. https://doi.org/10.1016/j.cemconres.2007.04.002.

70. Hay R, Li J, Celik K. Phase evolution, micromechanical properties, and morphology of calcium (alumino)silicate hydrates C–(A–)S–H under carbonation. Cem Concr Res. 2022. https://doi.org/10.1016/j.cemconres.2021.106683.
71. Shah V, Scrivener KL, Bhattacharjee B, et al. Changes in microstructure characteristics of cement paste on carbonation. Cem Concr Res. 2018. https://doi.org/10.1016/j.cemconres.2018.04.016.
72. Steiner S, Lothenbach B, Proske T, et al. Effect of relative humidity on the carbonation rate of portlandite, calcium silicate hydrates and ettringite. Cem Concr Res. 2020. https://doi.org/10.1016/j.cemconres.2020.106116.
73. Sun C, Liu L, Du Y. Analyses of decalcification process of calcium silicate hydrate (C-S-H) phase. IOP Conf Ser: Mater Sci Eng. 2019. https://doi.org/10.1088/1757-899X/490/2/022050.
74. Trapote-Barreira A, Cama J, Soler JM. Dissolution kinetics of C–S–H gel: flow-through experiments. Phys Chem Earth. 2014. https://doi.org/10.1016/j.pce.2013.11.003.